

Strain Sensing Sheets for Structural Health Monitoring Based on Large-Area Electronics and Integrated Circuits

This paper describes innovative sensing sheets for spatial mapping of surface strain and crack damage. The flexible substrates include a full integration of an array of strain sensors along with digital circuitry for power harvesting and signal processing.

By BRANKO GLIŠIĆ, YAO YAO, SHUE-TING E. TUNG, SIGURD WAGNER, *Fellow IEEE*, JAMES C. STURM, *Fellow IEEE*, AND NAVEEN VERMA, *Member IEEE*

ABSTRACT | Accurate and reliable damage characterization (i.e., damage detection, localization, and evaluation of extent) in civil structures and infrastructure is an important objective of structural health monitoring (SHM). Highly accurate and reliable characterization of damage at early stages requires continuous or quasi-continuous direct sensing of the critical parameters. Direct sensing requires deploying dense arrays of sensors, to enhance the probability that damage will result in signals that can be directly acquired by the sensors. However, coverage by dense arrays of sensors over the large areas that are of relevance represents an enormous challenge for current technologies. Large area electronics (LAE) is an emerging technology that can enable the formation of dense sensor arrays spanning large areas (several square meters) on flexible substrates. This paper explores the requirements and technology for a sensing sheet for SHM based on LAE

and crystalline silicon CMOS integrated circuits (ICs). The sensing sheet contains a dense array of thin-film full-bridge resistive strain sensors, along with the electronics for strain readout, full-system self-powering, and communication. Research on several stages is presented for translating the sensing sheet to practical SHM applications. This includes experimental characterization of an individual sensor's response when exposed to cracks in concrete and steel; theoretical and experimental performance evaluation of various geometrical parameters of the sensing sheet; and development of the electronics necessary for sensor readout, power management, and sensor-data communication. The concept of direct sensing has been experimentally validated, and the potential of a sensing sheet to provide direct sensing and successful damage characterization has been evaluated in the laboratory setting. A prototype of the sensing sheet has also been successfully developed and independently characterized in the laboratory, meeting the required specifications. Thus, a sensing sheet for SHM applications shows promise both in terms of practicality and effectiveness.

KEYWORDS | Civil structures and infrastructure; CMOS integrated circuits (ICs); damage detection and localization; hybrid system; large area electronics (LAE); strain sensing sheet; structural health monitoring (SHM)

Manuscript received March 15, 2015; revised February 7, 2016; accepted May 19, 2016. Date of publication June 23, 2016; date of current version July 15, 2016. This work was supported in part by the National Science Foundation under Grants ECCS-1202168 and CCF-1218206; the U.S. Department of Transportation, Office of the Assistant Secretary for Research and Technology, University Transportation Center (USDOT-RITA UTC) Program under Grants DTRT12-G-UTC16 and DTRT13-G-UTC28 enabled through the Center for Advanced Infrastructure and Transportation (CAIT) at Rutgers University; and Princeton Institute for the Science and Technology of Materials (PRISM).

B. Glišić and **Y. Yao** are with the Department of Civil and Environmental Engineering, Princeton University, Princeton, NJ 08544 USA (e-mail: bglicic@princeton.edu; yaoyao@princeton.edu).

S.-T. E. Tung was with the Department of Civil and Environmental Engineering, Princeton University, Princeton, NJ 08544 USA. She is now with Pankow Builders Ltd., Pasadena, CA 91101 USA (e-mail: ellen.tung@gmail.com).

S. Wagner, **J. C. Sturm**, and **N. Verma** are with the Department of Electrical Engineering, Princeton University, Princeton, NJ 08544 USA (e-mail: wagner@princeton.edu; sturm@princeton.edu; nverma@princeton.edu).

Digital Object Identifier: 10.1109/JPROC.2016.2573238

0018-9219 © 2016 IEEE. Personal use is permitted, but republication/redistribution requires IEEE permission. See http://www.ieee.org/publications_standards/publications/rights/index.html for more information.

I. INTRODUCTION

Structural health monitoring (SHM) is a process aimed at providing accurate and timely information concerning

structural condition and performance [1]. It is also referred to as the process of implementing strategies and systems for structural damage identification [2]. It requires permanent continuous, periodic, or periodically continuous recording of representative parameters from a monitored structure over short or long periods, as well as transforming the collected data into information on structural health condition and performance [1]. Fundamentally, the parameter of greatest interest in civil structures and infrastructure is stress. The reason is that structural materials fail when the stress reaches yielding point or exceeds the strength of the material. Unfortunately, there are no practical means to monitor stress in a real-world structure. On the other hand, strain is directly correlated with stress, making it an important parameter to monitor in SHM applications. Any change in the stress field (e.g., due to damage) implies a change in the strain field, which can be detected by an appropriate strain-sensing SHM system. Thus, in this paper, the focus is on strain as the primary monitoring parameter, and this choice is further supported in the following sections.

Ideally, SHM should enable the following actions [3]: 1) detection of unusual behavior (e.g., caused due to damage) in structures (so-called “level I SHM”); 2) indication of the physical location originating the unusual behavior (i.e., so-called localization of damage or “level II SHM”); 3) quantification of the extent of the unusual behavior and its origin (so-called “level III SHM”); and 4) actionable assessment of the structural health and structural performance (so-called prognosis or “level IV SHM”). Detection, localization, and quantification (level III SHM) of early-stage damage is of particular interest, as it enables prognosis (level IV SHM) and, consequently, optimization of repair and maintenance activities to ensure preservation of the structure and extension of its life span.

Early-stage damage frequently occurs in the form of local strain-field anomalies. Typical examples are bowing and cracking of steel (which are early indicators of loss of local stability and fatigue), as well as various types of crushing and cracking in concrete (which are early indicators of overloading and/or damage caused by frost, alkali reaction, and corrosion in reinforced bars). Today, only level I SHM is achievable (some successful examples are given in [1] and [5]), and even this is only partially and in specific applications. Early-stage level II and III SHMs are rarely achieved in practical settings today (some successful examples are given in [1], [7], and [8]). Hence, the research presented in this paper focuses on monitoring strain-field anomalies as a means of achieving reliable and accurate level III SHM, i.e., reliable and accurate damage detection, localization, and evaluation of damage extent.

The aim of this paper is to explore the requirements and technology for creating a novel 2-D sensor, called sensing sheet, which will enable identification of strain-field anomalies over large structural areas and achievement of level III SHM in real-life settings. The presented

research includes several stages for translating the sensing sheet to practical SHM applications. Section II introduces the concept of direct sensing, Section III presents experimental characterization of an individual sensor as well as theoretical and experimental performance evaluation of various geometrical parameters of the sensing sheet, and Section IV develops the electronics necessary for sensor readout, power management, and sensor-data communication. The paper closes with Section V, where conclusions and future work are presented. The original contribution of this paper lays in holistic analysis of all stages of the research, which led to important conclusions that could not necessarily be inferred from separate analysis of each individual stage.

II. DIRECT-SENSING APPROACH

A. Real-World Example Motivating Direct Sensing

The direct-sensing approach involves either direct contact or close proximity of sensors with damage. This is referred to as direct sensing because it enables a discernably large change in the output of the sensors in response to relevant damage. Thus, it is necessary that the observed parameter (measured by the sensor) at location of damage can be significantly altered by the damage (examples of parameters that enable direct sensing are strain, electrical impedance, parameters related to mechanical wave propagation, etc.). Since the likely locations of damage within a structure can only be predicted with limited accuracy, direct sensing requires deployment of dense arrays of sensors, yet with coverage over large areas of the structure where damage may be expected. Provided this, studies show that the great advantage achieved with direct sensing is very high reliability in damage detection and localization, as well as excellent accuracy in evaluation of damage extent [4].

As mentioned, however, technologies available today cannot practically provide direct sensing. Dense arrays of sensors imply high hardware and deployment costs, as well as complex data management. Thus, systems for SHM today are mostly based on indirect sensing, using a significantly smaller number of sparsely placed sensors. The primary drawback of this approach is its reliance on elaborate data-analysis algorithms for extracting damage-characterization information. In practice, the reliability of such methods faces major challenges in the presence of practical environmental influences (i.e., variations in temperature and humidity) and typical variances in loading conditions [5].

Fig. 1 provides a comparison between direct and indirect sensing using a practical example [6]. The Streicker Bridge is a footbridge on the Princeton University campus. This structure has been equipped with an SHM system based on long-gauge fiber optic sensors, having gauge length of 60 cm [4], [6], [7]. In particular, cross-section P10h11 contains three sensors, P10h11U,

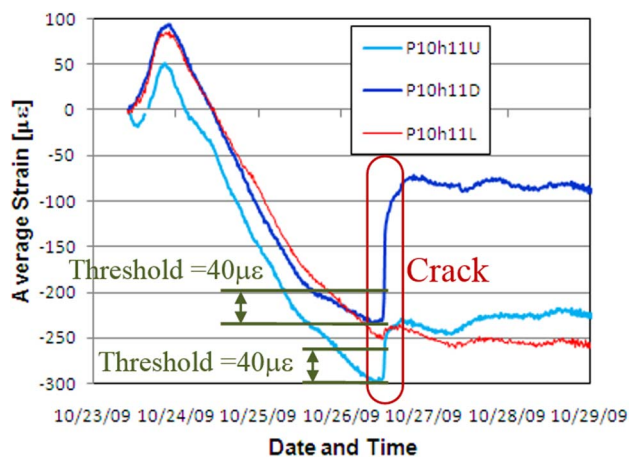


Fig. 1. Example of direct damage (crack) detection in real-life settings (example taken from Streicker Bridge [6]).

P10h11D, and P10h11L, all three embedded in the concrete deck. Early-age cracking occurred in the section P10h11 in the area of sensors P10h11U and P10h11D. As shown, the associated sensors are strongly activated, resulting in clearly discernible changes in strain reading, i.e., at least order of magnitude higher than both the resolution of the SHM system and the typical background variations observed due to normal temperature and loading. Hence, these sensors directly detect and localize the crack, and the strain measurements provide substantial information to quantify the crack [4]. At the same time, the sensor P10h11L, whose position was in fact less than 1 m away from the cracking zone, did not register a change in stain that could be reliably discerned in the presence of the normal background variation (i.e., the small change observed is within the range of typical temperature and loading variations, making damage characterization difficult to achieve).

While this example highlights the inability of indirect sensing to reliably provide damage information, taking the three sensors as a modest array, it becomes possible to see the level of information that can be extracted if a dense sensing-array technology were available.

Fig. 2 shows strain in a steel plate as a function of distance from the point of crack initiation (example taken from the tests presented in Section III-D). Diagram shows that the strain magnitude degrades rapidly with distance from the crack initiation point. Thus, initial stages of damage would not be detected by sensors that are even just a few centimeters away. Conversely, it could be noticed that because strain magnitudes at and around the location of crack initiation are substantially higher than at distances away from the crack, accurate detection and localization can be achieved.

Both direct and indirect sensing have various advantages and challenges, as discussed in [7] and [8]. However,

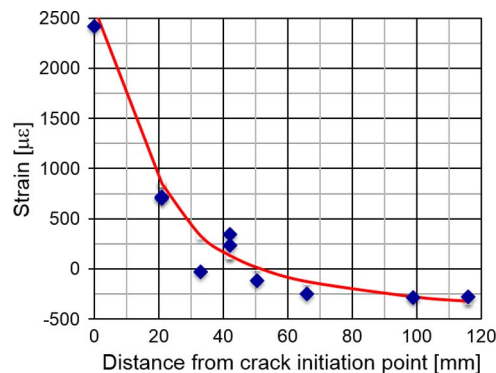


Fig. 2. Example of strain distribution as a function of distance from strain crack initiation point.

the crucial advantage of direct sensing is the acquisition of high-quality signals, overcoming the need for complex algorithms, making it possible to achieve high reliability in damage characterization (detection, localization, and evaluation of damage extent) in practical settings.

B. Need for 2-D Strain Sensing

Currently available technologies offer three classes of strain sensors: discrete short-gauge sensors [e.g., strain gauges, vibrating wire sensors, and fiber Bragg grating (FBG) sensors], discrete long-gauge sensors (low coherence interferometric sensors, specially packaged FBG sensors, or intensity-based fiber optic sensors), and continuous (1-D) distributed sensors (sensing cables based on Brillouin or Rayleigh scattering). The damage detection performance of these three classes of sensors is conceptually compared in Fig. 3 considering their direct-sensing capabilities in a given configuration. The figure shows that, for short-gauge, long-gauge, and 1-D distributed sensors, the reliability of damage detection increases with spatial coverage of the structure, i.e., it is lowest for short-gauge and the highest for 1-D distributed sensors.

Fig. 3 also illustrates the need for 2-D distributed sensors. Assuming that the locations of all types of damage cannot be accurately predicted, which is often the case in practical settings, short-gauge, long-gauge, or 1-D distributed sensors are likely to miss the areas where the damage actually occurs (e.g., the locations E1 and E2 in the figure). This motivates the need for a sensing technology with greater spatial coverage, namely 2-D distributed sensing.

The benefits of the direct-sensing approach, and the need for various forms of 2-D distributed sensing, have indeed been recognized in several studies. These include self-sensing cementitious materials [9], various types of sensing skins based on nanomaterials [10]–[13], nanopaints [14], conductive polymers [15], photonics crystals [16], and expandable electronics [17].

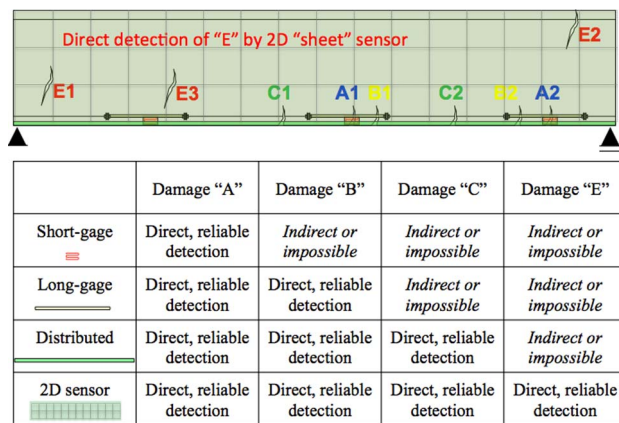


Fig. 3. Conceptual comparison between damage detection performances of short-gauge, long-gauge, and 1-D distributed sensors used in direct-sensing approach, and illustration of the need for 2-D sensing sheets [4].

Large area electronics (LAE) combined with CMOS integrated circuits (ICs) into a hybrid system called sensing sheet [6], [18]–[21] has been identified by researchers at Princeton University as an emerging technological solution that has potential to address the technical and deployment challenges of large-scale direct sensing, the ability to enable cost-viable solutions scalable to the size of civil structures and infrastructure, and the possibility of providing early-stage level III SHM.

C. LAE as Technological Enabler for 2-D Strain Sensing

LAE is based on processing thin-films at low temperatures (< 200 °C). Low-temperature processing has two characteristics. First, it enables compatibility with a wide range of materials, making possible the formation of diverse transducers for sensing and energy harvesting [22]. Second, it enables compatibility with substrates such as glass and plastics, which can be large (on the order of square meters) and flexible. This makes LAE a potentially transformational technology, enabling coupling to physical sources of signals and energy on a scale that far surpasses existing technologies. Indeed, LAE research over the past ten years has led to an extremely rich set of demonstrated sensors and energy harvesters. On the sensors side, typical examples are strain sensors [23], pressure sensors [24], mechanical force sensors [25], and on the energy harvesters side, typical examples are solar harvesters, thermal harvesters, and mechanical harvesters [26].

However, to address SHM applications, a practical system requires functionality in addition to sensing. In particular, this includes instrumentation, to readout sensor data; computation, to perform local data processing and analysis; power-management, to enable autonomous operation over extended periods; and communication, to transmit data and analysis outputs to centralized sources.

Table 1 Comparison of the Electrical Parameters of LAE TFT and Silicon MOSFETs

Symbol	a-Si LAE TFT	MOSFET IC (130 nm)
Mobility (μ_e)	μ_e : 2 cm ² /Vs	μ_e : 1000 cm ² /Vs
$t_{\text{dielectric}}$	280 nm	2.2 nm
V_{DD}	6 V	1.2 V
$C_{\text{GD/GS}}$	3.3 fF/ μm	0.34 fF/ μm
f_T	1 MHz	150 GHz

Such functionality is realized through circuits formed from transistors. While LAE does enable the formation of low-temperature thin-film transistors (TFTs), these have electrical performance and energy efficiency that is far below that of the transistors available in typical electronic systems based on silicon CMOS ICs. Silicon CMOS ICs involve processing at high temperatures (> 1000 °C). This precludes the benefits enabling the sensors and energy harvesters in LAE, but it results in orders-of-magnitude higher transistor performance. For illustration, Table 1 compares the key parameters of silicon CMOS transistors fabricated in a typical 130-nm technology with those of TFTs fabricated in an amorphous-silicon (a-Si) technology, which is the work-horse LAE technology used for large flat-panel displays today [27]. The parameters summarized are as follows: μ_e is the mobility of electron current carriers, which specifies how fast carriers move through a material subjected to electric field, e.g., via application of a voltage; $t_{\text{dielectric}}$ is the gate-dielectric thickness, which determines how many current-causing carriers are generated as a result of a voltage applied to the transistor’s input electrode, i.e., gate; V_{DD} is the typical supply voltage, which sets the energy required to perform circuit functions; $C_{\text{GD/GS}}$ are the gate-drain/-source electrode capacitances, which both limit the speed of internal signals and determine the energy consumed as a result of the amount of electric charge that must be involved in voltage transitions; and f_T is the unity current-gain frequency, which specifies the maximum frequency at which a transistor provides more output current than it sinks input current (often regarded as the maximum frequency at which the transistor is usable).

Given the disparity shown in Table 1, the TFTs available in LAE are likely to result in systems that are highly suboptimal, limited in scalability, or both. LAE and CMOS ICs provide fundamentally different materials, leading to corresponding functional advantages and disadvantages. To create a sensing sheet, which can provide both the level of sensing required in SHM applications and the surrounding functionality necessary to realize a practical system, this paper explores a hybrid approach, combining LAE with CMOS ICs. The demonstrated prototype shows promise toward addressing the challenges faced in SHM applications.

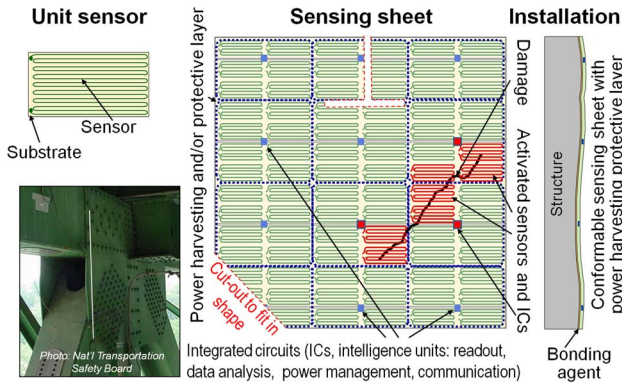


Fig. 4. Concept of the sensing sheet and its application [19].

III. SENSING SHEET REQUIREMENT ANALYSIS

A. General

The three principal components of the sensing sheet are [6]: 1) a dense 2-D array of unit strain sensors patterned (using metal deposition and etching) on a polyimide substrate along with functional LAE (including power converters); 2) embedded ICs interfaced via noncontact links for sensor readout, data processing and analysis, power management and communication; and 3) integrated flexible photovoltaics for power harvesting. The sensing sheet components and the principle of damage detection are schematically represented in Fig. 4.

Damage is detected by sensors that are directly activated (shaded in Fig. 4), and whose output strain signal is significantly higher than that of other sensors not in direct contact with the damage. Damage location and extent are determined by coordinates (locations) of activated sensors (see Fig. 4). Thus, the damage detection capability of the sensing sheet depends on the performance of the unit sensors when exposed damage, and on the geometrical arrangement of unit sensors within a dense array. These aspects are analyzed in the following sections.

B. Physical (Unit) Sensor Exposed to Damage

Generally, any available electrical sensing technique can be used for the unit sensors. However, full-bridge resistive strain sensing is selected due to its established use in SHM, and it has well understood and proven attributes. A full-bridge sensor consists of four resistors, each patterned in form of a multiple serpentine, to improve sensitivity and accuracy. The resistors are oriented in two perpendicular directions and interconnected in a Wheatstone bridge configuration, as shown in Fig. 5. Such a sensor provides a differential strain signal, which significantly improves robustness against external influences. In particular, temperature variations affect all four resistors in approximately the same manner, and

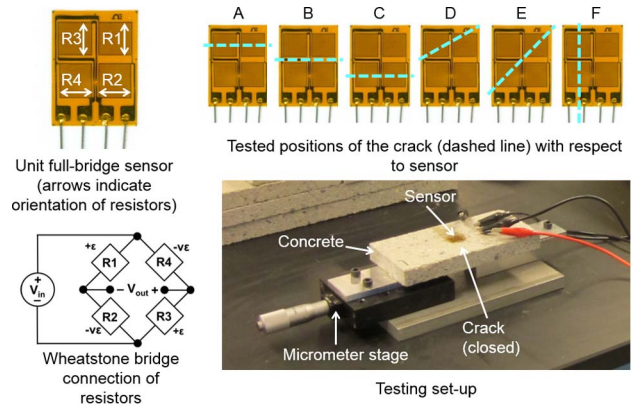


Fig. 5. Full-bridge sensor (top-left), Wheatstone bridge (bottom-left), tested configurations of sensors (top-right), and testing setup (bottom-right).

differential reading (which subtracts reading of transversal resistors from the reading of longitudinal resistors) provides with thermal compensation of the sensor (influence of temperature variations was measured to be around $-1 \mu\epsilon/^\circ C$, which is practically negligible for the purposes of damage detection).

The sensing sheet is intended to be glued onto the surface of monitored structure, and each individual strain sensor is expected to measure the strain in the construction material. In general, two scenarios can occur. First, there is no damage in form of cracks in the construction material (typically concrete or steel); in this case the unit sensors are expected to simply measure the strain in the material. Second, there is a crack in construction material; in this case the sensor is expected to either fail or to “survive” the crack and, in the latter case, measure the strain induced by the crack opening.

The sensing sheet is fabricated on a polyimide substrate, i.e., the same substrate commonly used in foil strain gauges. Since the strain gauge is a proven sensor, and strain transfer from the construction material to the sensor is also well proven, the first scenario is not of interest in this study, as direct analogy with traditional strain gauges can be made. However, behavior of the unit sensor exposed to damage is not well known, and is thus studied in further detail in this section.

As a starting point, testing of the unit sensor was performed using commercially available full-bridge resistive strain sensors. This is expected to provide useful characterization results for the eventual sensing sheet, since it will employ manufacturing procedures for the unit strain sensors that are similar to those employed for the sensors commercially available today.

The unit sensors were tested under repeatable laboratory conditions as follows. A crack was artificially created on a small concrete slab, which was then fixed to a micrometer stage. In this way, the crack width could be

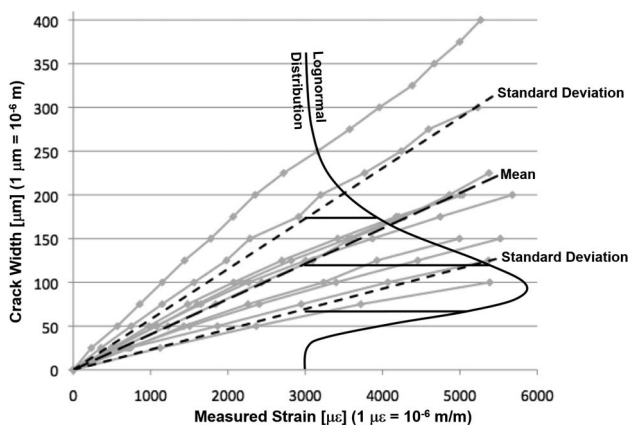


Fig. 6. Crack width versus measured strain for tests in configuration “A” (modified from [19]).

controllably adjusted (i.e., the crack closed or opened) using the stage. The unit sensor shown in Fig. 5 (gauge length = 7.4 mm) was bonded to the plate over a closed crack. Once the glue was hardened, the crack was opened using the stage, its width was incrementally increased until the sensors failed, and the sensor output was registered at every increment. In total six different positions of crack with respect to sensor were tested. Fig. 5 shows the testing setup and tested crack positions.

The configuration “A” (see Fig. 5) was tested ten times, in order to have certain statistics on sensor behavior under the crack condition. As the tests were time consuming, all other configurations were tested only three times, which was judged as sufficient to achieve the aims of tests. Tests have demonstrated that the unit sensor installed on concrete can survive a crack width of 1.5 mm, on average. This was possible mostly due to degradation of concrete at the crack mouth which enabled redistribution of high local strain (generated by crack) over the longer length of the sensor [19].

Fig. 6 shows diagram crack width versus measured strain as registered in ten tests with configuration “A” from Fig. 5 (crack perpendicular with respect to resistors R1 and R3) [19]. The strain measured by the sensor is a combination of the zero strain due to the portion of the sensor, which is in direct contact with concrete, and the highly concentrated strain due to the portion of the sensor that was delaminated from the concrete at the location of the crack opening. While the slope of the resulting regression line between the crack width and the measured strain was not the same in each test, it was found that it follows lognormal distribution, and thus the crack width could be estimated in a statistical manner (i.e., within a confidence interval) rather than in a deterministic manner. The distribution is lognormal rather than normal, i.e., it is skewed, because the crack always results in a positive readout change (crack never causes negative reading on the sensor). The dispersion in results

from different tests is consequence of several uncontrollable factors such as thickness of the adhesive, local defects in the concrete, exact shape of the crack, and probable variations in sensors’ electrical and mechanical properties.

Configurations “A,” “B,” and “D” all had similar responses. The slope of the regression line of configuration “C” was approximately two times lower that for configuration “A,” while that of “F” was negative, with magnitude similar to “C.” Finally, configuration “E” had regression slope close to zero (i.e., the strain signal from two activated resistors in the bridge cancels out); thus this configuration is considered the least favorable. However, in the case that one or few sensors in the sensing sheet are exposed to a crack in this configuration, the crack is likely to be detected indirectly by other neighboring sensors, as shown in Section III-D.

C. Modeling Response of Multisensor Array

The sensing sheet eventually consists of densely spaced sensors; however, the sensors cannot be patterned immediately next to each other due to the need for control and accessing circuitry. Thus, empty spaces between the sensors will exist. These noninstrumented spaces are not directly sensitive to damage, and this may adversely affect the reliability of damage detection. Thus, it is necessary to study the influence of the sizes and shapes of the noninstrumented areas. This will lead to general guidelines on the most efficient arrangement of the sensors in the sensing sheet, i.e., on the most efficient geometrical design of the sensing sheet.

The geometrical design of the sensing sheet is studied based on probability of detection (POD). POD is a practical metric used broadly to quantify the reliability of inspection systems. Applied to SHM, it represents the probability of correct detection of damage of a given size [28]. For example, let us assume that the sensing sheet with dimensions $W \times L$ contains only one sensor with dimensions $w \times l$. These parameters are illustrated in the left image of Fig. 7. Let us further assume that the crack is detected if it has at least one common point with the sensors (i.e., touches or intersects the sensor, e.g., cracks c_2 and c_3 in left image of Fig. 7), and, further, false positive and false negative detections are not possible (i.e., the sensor functions with perfect reliable). Finally, let us assume that the crack can be represented as a segment of the line with length c , and that its probability of occurrence within the sensing sheet is uniform.

Given these assumptions, the POD can be computed [29], for any specific size of sensing sheet, size of unit sensor, its position within the sensing sheet and crack length. For a single sensor placed in the center of the sensing sheet (case “A” in Fig. 7), analytical solution can be found in closed form [29]; however, for nonsymmetric cases and cases with multiple sensors in the sensing sheet, the analytical solution becomes difficult to derive.

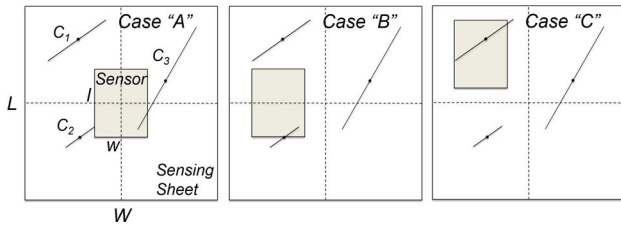


Fig. 7. Schematic representation of design parameters of sensing sheet with one unit sensor; three typical positions of the unit sensor within the sheet are presented.

In these cases, Monte Carlo simulation (MCS) is used. Fig. 8 shows examples of POD calculated for three cases shown in Fig. 7, for $W \times L = 40 \text{ mm} \times 40 \text{ mm}$, and $w \times l = 11 \text{ mm} \times 14 \text{ mm}$.

For case “A,” analytical and numerical (MCS) solution are presented in Fig. 8, showing good agreement with each other. This provides confidence in the MCS approach and its suitability for calculating POD. For a crack length of 0 mm, the POD is simply equal to the ratio between the sensor area and the sheet area.

Fig. 8 shows two important findings. The first finding is that for a given design of the sensing sheet, POD increases with increasing size of the crack; however, after a certain size of crack is reached (called critical crack length), the POD becomes constant. This is practically the maximum POD that can be achieved by a given design of the sensing sheet. The second finding is that the POD depends on the position of the unit sensor within the sensing sheet, and the maximum POD is achieved with a symmetric configuration, i.e., when the sensor is placed symmetrically with respect to both horizontal and vertical axes. This is explained as follows. It is assumed that the sensor can detect the crack only when in direct contact with it, thus for a given crack length l there is an $l/2$ wide band around the sensor that defines geometrical positions of centers of the cracks that could be detected. If the sensors is not placed in the center of the sheet, part of the band will be out of the sheet, and this reduces its capability to detect the damage, i.e., POD decreases. Detailed analysis of this phenomenon can be found in [29].

These findings were verified and found to be valid for a sensing sheet with multiple sensors [29]. In addition, it was found that the sensors must be mutually equidistant in both directions to achieve maximum POD, as shown in Fig. 9 for a sensing sheet containing 4, 9, and 16 sensors.

Fig. 10 shows POD calculated using MCS for the three cases shown in Fig. 9 ($W \times L = 90 \text{ mm} \times 90 \text{ mm}$, $w \times l = 11 \text{ mm} \times 14 \text{ mm}$).

Three important findings result from Fig. 10. First, all curves have behavior similar to that in Fig. 8, i.e., PODs start from value determined as ratio of combined

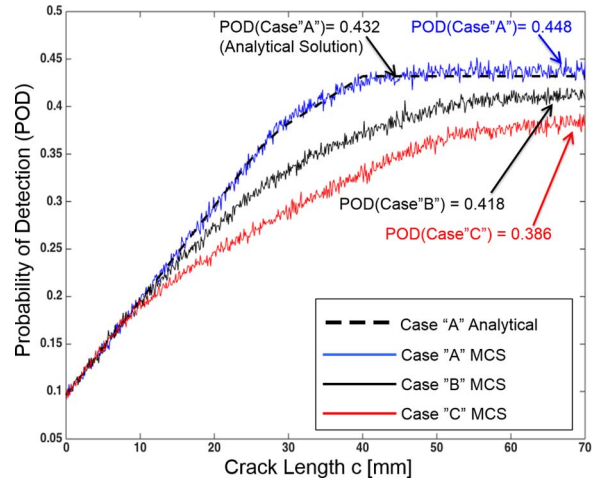


Fig. 8. POD for the three designs of sensing sheet shown in Fig. 7; for case “A” two solutions are presented, analytical and numerical (MCS).

sensor area over the sheet area, they have steep linear increase for shorter crack lengths, and they asymptotically approach the maximum POD for longer crack lengths; and they all reach a maximum POD for a certain crack length, called critical crack length and denoted with c_{cr} . The second finding is that the critical crack length decreases as the number of sensors increases (e.g., for example in Fig. 9 the values are $\sim 69 \text{ mm}$ for four-sensor scenario, $\sim 50 \text{ mm}$ for nine-sensor scenario, and $\sim 36 \text{ mm}$ for 16-sensor scenario). Finally, the third finding is that the maximum POD is greater for a sensing sheet that contains more sensors, which is expected, since a larger area of the sheet is covered with sensors.

The evaluation of POD presented in this section deals with a single crack of a given size. If POD of multiple cracks is of interest, it can be calculated using the probabilistic formulas for multiple events (for example, if detection of several, mutually independent, cracks of a given length is of interest, then the POD of all of them is calculated as the product of their individual PODs, etc.).

In general, the POD results presented in this paper can be applied to the cases of damage that geometrically manifests in form of lines or systems of lines (e.g., cracks

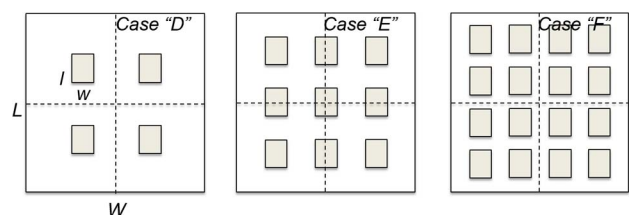


Fig. 9. Schematic representation of sensing sheets with the same dimensions and equidistantly spaced 4, 9, and 16 sensors.

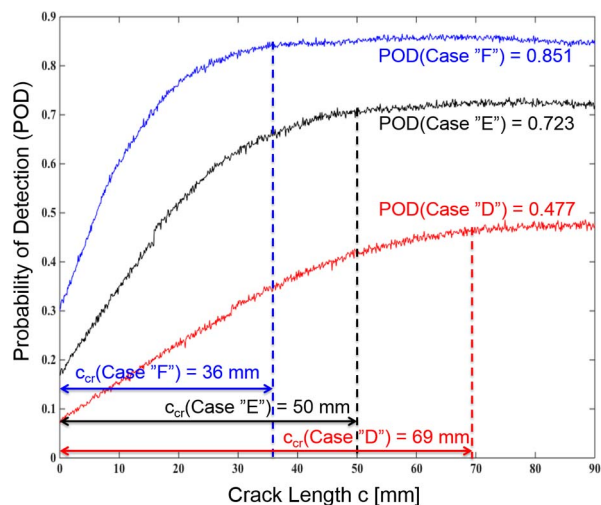


Fig. 10. POD for the arrangements of sensors shown in Fig. 9.

or local bowing). To evaluate the POD for other types of damage, similar procedure as presented in this paper can be applied, but geometrical manifestation of the target damage has to be taken into account.

D. Experimental Validation

The modeling of the sensing sheet presented above is based on idealized assumptions, with the aim to gaining general insights. Of course, the assumptions outlined in the previous subsection may not be fulfilled in real-life settings. Hence, to assess and validate the sensing sheet capabilities in terms of damage detection, localization and quantification, a series of tests were performed in the laboratory.

The tests consisted of cyclic loading of steel plates instrumented with sensing sheet prototypes, as shown in Fig. 11. The plates had a notch on the boundary leading to the generation of a fatigue crack under cyclic loading. The crack occurrence and propagation was monitored using sensing sheets. Since the point of occurrence of the crack (at the notch) and its approximate propagation (perpendicular to the applied force) were known (see Fig. 11), it was decided to test two arrangements of unit sensors within the sensing sheet.

The first arrangement of sensors, called design 1, consisted of a moderately dense array of sensor as shown in Fig. 11. This array consisted of the main grid of equidistantly spaced sensors (see Fig. 11), and a secondary grid whose aim was to assess the influence of the crack on the sensors that are in close proximity to the damage, but not directly intersecting it. The total size of the sensing sheet was 150 mm × 150 mm (6 in × 6 in), and the total number of unit sensors was 31 (11 mm × 14 mm each).

The second arrangement of sensors, called design 2, consisted of a very dense array of sensors concentrated in the area of the expected crack (see Fig. 11). The sensors were in a staggered configuration (rather than

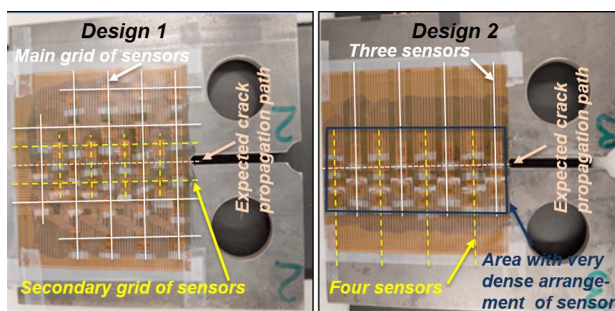


Fig. 11. View to plates instrumented with sensing sheets; design 1 (left) had moderate density of sensors, and design 2 (right) had high density of sensors in the area of crack occurrence.

equidistantly spaced). The reason for this is that, in assumptions presented in Section III-C, the sensors were assumed to have the same sensitivity to damage in all directions; however, the tests presented in Section III-B suggested that this is not true for practical full-bridge sensors. Hence, a staggered configuration was employed in order to get response from two relative positions of crack with respect to sensor, i.e., to realize configurations “A” and “C” shown in Fig. 5. More precisely, the middle sensor in each row with three sensors (see Fig. 11) was expected to be in configuration “A” from Fig. 5, while the second sensor from the top of each row with four sensors was expected to be in configuration “C,” as rows with four sensors were staggered with respect to rows with three sensors. The total area covered by sensors was 150 mm × 55 mm (6 in × 2.2 in) and total number of sensors was 28.

For these initial tests, a sheet consisting of unit sensors was fabricated, rather than a fully integrated sensing sheet, and a readout unit based on commonly available equipment was used, rather than the eventual LAE and CMOS ICs. Thus, commercially available full-bridge sensors, the same as described in Section III-B (see Fig. 5), were laminated over a sheet of copper interconnects, the latter being specially designed and manufactured for the desired configurations. This resulted in a setup enabling key experiments, providing good representation of the eventual sensing sheet. Resistors R1 and R3 of each sensor were oriented perpendicular to the expected crack propagation line, while the resistors R2 and R4 were oriented parallel to the crack propagation line. Adhesive, installation procedure, and strain transfer of sensing sheet were laboratory tested before the application on the steel plates.

Four fatigue cycling tests were performed, two involving the sensing sheet of design 1, and two the sensing sheet of design 2. The loading range was different in the different tests, with a typical range between 53 kN (12 kip) and 125 kN (28 kip). The plate under test was considered as failing when the displacement between the

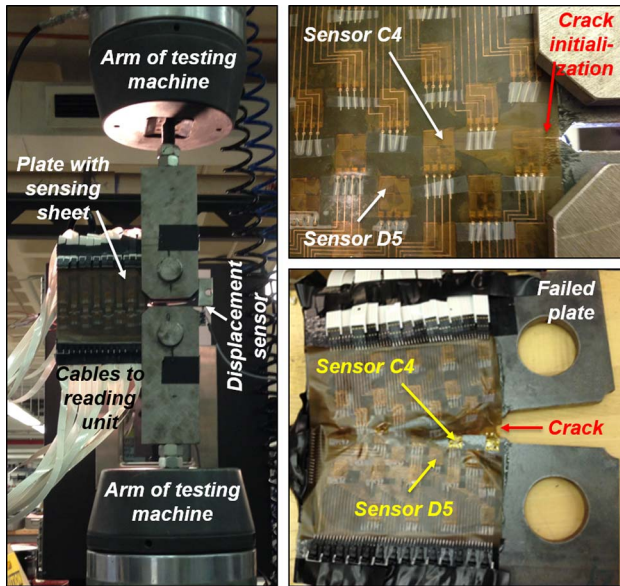


Fig. 12. Views to testing setup (left), crack initialization (upper right), and failed plate with sensing sheet of design 1 (lower right).

arms of the testing machine reached 25.4 mm (1 in). Sampling rate of unit sensors was 20 Hz. Detailed description of the tests is given in [30].

The initiation of the crack in each plate occurred in less than 40000 cycles. Further cycling caused slow propagation of the crack through the plate, and rapid acceleration when the plate was close to failure. Fig. 12 shows the testing setup with the sensing sheet of design 1, illustrating crack initiation and a failed plate.

Two representative patterns of readings from unit sensors were registered. The first is a reading from a sensor that intersects the crack, and the second is a reading from a sensor that is close to the crack. Examples of such sensors are C4 and D5 shown in Fig. 12. Their readings are shown in Fig. 13. Distinct stages related to crack propagation are shown in the figure.

Four important conclusions can be drawn from the results. First, both sensors were able to detect the crack propagation, i.e., to predict that the crack length is increasing and the crack path is “approaching.” Second, the sensors that were in direct contact with the crack (e.g., sensor C4) failed almost immediately after they were intersected by the damage, and this failure can be used effectively to detect the crack. The failed sensors exhibit behavior which is different from that presented in Section III-B. The reason for this difference in the two tests is that the crack mouths in the case of steel do not degrade upon the crack occurrence, unlike concrete where the crack mouths do degrade. This lack of degradation prevents stress relaxation in the sensors, leading to their failure. Third, even sensors that are not in direct contact with the crack, but close enough to it (e.g.,

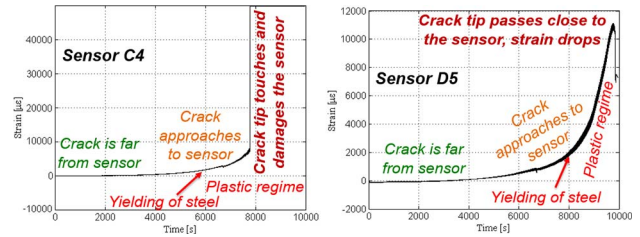


Fig. 13. Typical measurements recorded by sensor located onto a crack path (left) and close (but not onto) a crack path (right).

sensor D5), can detect the damage through a sudden change in strain trend (e.g., decrease in strain observed in Fig. 13 as a consequence of crack; strain decreases at and around the crack mouth because the tension in material is lost due to crack opening). This suggests that the POD of the sensing sheet may actually be higher than that predicted in Section III-C. Fourth, actually a consequence of the previous three conclusions is that for uniaxial dominant strain distribution a material, the position of the crack with respect to the sensor, does not play a major role in crack detection capability. In the other words, the crack would be detected regardless of its orientation with respect to the sensor (i.e., in all configurations “A” to “F” shown in Fig. 5). The detection would be in the form of either high strain and/or failed sensors in direct contact with the crack (see left image of Fig. 13) or by sensors close to the crack registering large rise and drop in strain (see right image of Fig. 13). The first aforementioned conclusion is specific to the tested sensing sheet designs. The three other conclusions are more general, as they do not depend on the arrangement of sensors within the sensing sheets.

Based on the concept of POD described in Section III-C, a detectable threshold of crack length cannot be established in a deterministic sense. For a given configuration of the sensing sheet and given crack length, only a probability that this crack will be detected can be estimated. Moreover, POD never reaches value of 1, which means that even long cracks could be undetected. However, POD was based on the assumption that the crack is detected only if it is in physical contact with the sensor, while the tests have shown that the crack can be detected even if the crack passes nearby, but “close enough” to the sensor. This indicates that an appropriate spacing between sensors may lead to establishment of a minimum detectable crack length in a deterministic sense, which is a topic that will be addressed in future research (e.g., for the case shown in Fig. 2, the “close enough” spacing of sensors could be approximately $2 \text{ mm} \times 10 \text{ mm}$ to $2 \text{ mm} \times 20 \text{ mm} = 20\text{--}40 \text{ mm}^2$).

Based on the results from the unit sensors, 2-D time-history graphs are created and four characteristic examples are shown in Fig. 14. The results obtained in the other three tests were similar. Due to manufacturing

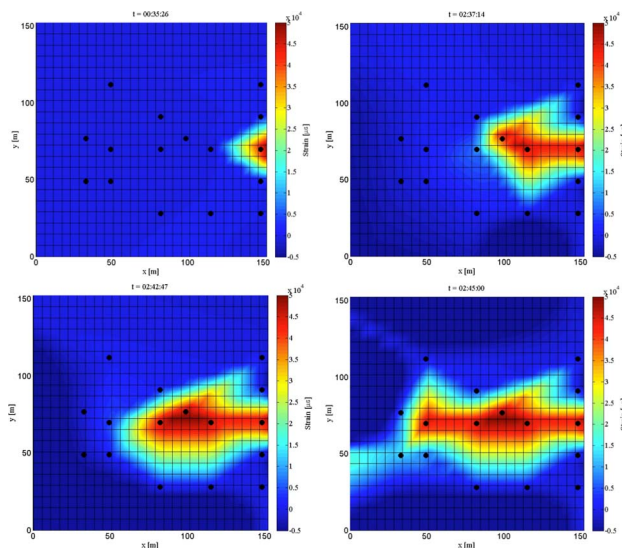


Fig. 14. Images of crack propagation obtained by interpolation of strain measurements taken from unit sensors (sensing sheet of design 1).

defects, several unit sensors lost electrical contact with their interconnects (10%–40% of sensors in different sheets), and thus could not be read out during the entire experiments. The graphs in Fig. 14 were created taking into account only fully functioning sensors, indicated in Fig. 14 as black circles. The strain values at point not directly instrumented were derived using linear interpolation. The upper left image shows the crack initiation, the upper right and lower left images show crack propagation, and the lower right image shows final crack extension at the completion of the test.

Two important conclusions are derived from Fig. 14. First, the sensing sheets were able to detect the crack initiation, follow its propagation, and evaluate its extension. Second, even though some sensors did not register strain due to manufacturing defects, the reminder of the sensors was sufficient to capture the critical characteristics of the damage. This demonstrates inherent redundancy and thus robustness of the sensing sheet for crack detection and characterization. Overall, the tests confirmed direct sensing to be an effective approach for damage detection and characterization. In addition, the tests validated the sensing sheet as a practical implementation of a dense array of sensors for damage detection and characterization.

IV. TECHNOLOGY DEMONSTRATION AND ANALYSIS

A. System Overview

The underlying principles, leading to a hybrid sensing sheet (i.e., combining LAE and CMOS ICs) for SHM applications, are discussed in detail in [21]. This section provides an overview of the prototype system, implemented to

explore the architectures by which the requirements developed in Section III can be met. To enable continuous sensing in the manner identified, the sensing sheet minimally consists of three subsystems: 1) sensing subsystem; 2) power-management subsystem; and 3) communication subsystem. An overview of these, starting with an overview of the overall approach, is provided below. Greater circuit and architectural details are provided in [27].

Starting from the basic technologies, whose electrical characteristics are summarized in Table 1, a large disparity in performance between the TFTs available in LAE and the transistors available in CMOS ICs is observed. This motivates architectures that generally aim to implement most functionality in the CMOS domain. As discussed in Section II-C, the primary functions to be implemented in the LAE domain are sensing and energy harvesting. However, with the large number of sensors targeted and the large physical dimensions over which they are distributed, the primary challenge is the *interfacing* needed between the LAE and CMOS domains. The large number of sensors necessitates architectures based on accessing schemes, such that acquisition can be performed through a minimal number of physical interfaces. The distributed nature necessitates multiple distributed CMOS ICs, which enables partitioning of the sensors into subarrays, each interfaced with a localized CMOS IC, to mitigate excessively long interconnects, which are likely to compromise the robustness of sensor acquisition and accessing control. This leads to the overall sensing sheet architecture shown in top image of Fig. 15. Distributed LAE subarrays are each coupled to a CMOS IC, and data as well as control information is communicated among the LAE/CMOS subarrays for coordinated operation over the entire sensing sheet.

The interfacing approach corresponding to such an architecture raises two key needs. First, within a subarray, acquisition from individual sensors requires LAE circuitry for scanning the sensors via a small number of interfaces. The circuitry employed is discussed in Section IV-B. Second, because the number of sensor subarrays can be large, a potentially large number of CMOS ICs must be coupled to the LAE sheet. Currently, no high-volume process exists to electrically bond large numbers of small ICs to large, flexible sheets. This motivates an approach based on *inductive* and *capacitive* noncontact coupling. Shown in bottom image of Fig. 15, this involves a flexible credit-card sized carrier on which planar inductors and capacitor plates are patterned, and to which each IC is bonded (similar to the assembly used for RFID tags). Corresponding inductors and capacitors are patterned on the large-area sheet, and the entire system is thus assembled through sheet lamination, avoiding the need for explicit metallurgical bonds. In the prototype described, the lamination adhesive is roughly 100 μm thick, enabling substantial capacitance density (100 pF/cm²) and inductive coupling factors.

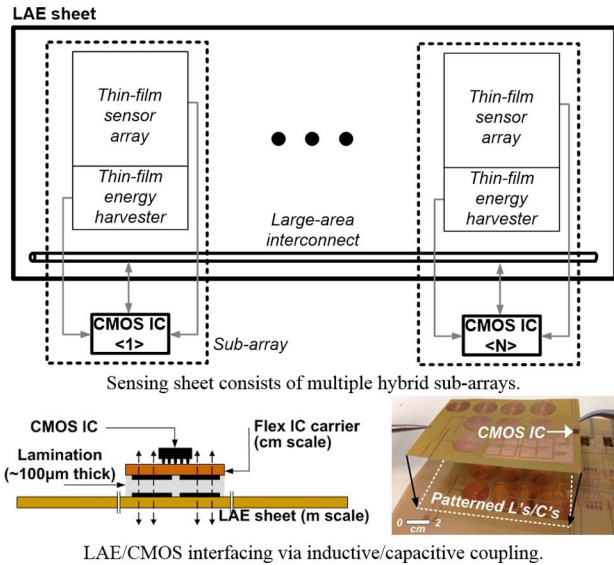


Fig. 15. High-level architecture of hybrid sensing sheet and LAE/CMOS interfacing strategy.

With the inductive and capacitive interfaces enabling functionality to be selectively distributed between the LAE and CMOS domains yet in a manner that is scalable over the entire system, Fig. 16 illustrates the overall architecture of a hybrid subarray. The subarray consists of three subsystems, each having an architecture driven by the use of inductive/capacitive interfacing. In the sensing subsystem, the LAE domain provides strain sensing and circuitry for sequential sensor accessing, and the CMOS domain provides instrumentation, A/D conversion, and sensor accessing control. In the power-management subsystem, the LAE domain provides solar energy harvesting and circuitry for power inversion (dc/ac conversion), and the CMOS domain provides rectification, over-/under-voltage monitoring, and dc/dc conversion/regulation. In the communication subsystem, the LAE domain provides long interconnects (0.1–10 m) for transmitting data, and the CMOS domain provides digital-data transceivers. Sections IV-B–IV-D present the design and implementation details of each subsystem. Following this, testing and characterization of the sensing sheet prototype is presented in Section IV-E, demonstrating a promising path to address the specifications for SHM applications.

B. Sensing Subsystem

The prototype sensing sheet consists of two options for the sensing subsystem [27]. The first employs strain sensors based on the mobility response of amorphous-silicon (a-Si) TFTs, while the second employs strain sensors based on the resistive response of thin-film metallization (copper–nickel alloy). The resistive sensors

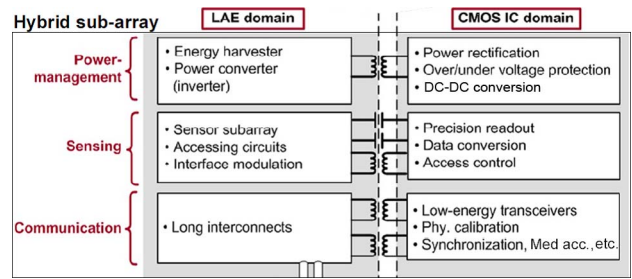


Fig. 16. Distribution of functionality between LAE and CMOS domains.

are the same as those characterized in Section III-B, and thus are the focus in this paper.

Fig. 17 shows the details of the hybrid sensing subsystem [27]. Sensor readout is performed by the CMOS IC by generating an ac bias voltage across the resistive bridge. Providing the bias voltage through inductive coupling has two benefits. First, a full-swing switching power amplifier can be employed by the CMOS IC to maximize efficiency, while exploiting the turns ratio of the coupling inductors to optimize the biasing current/voltage for the sensor resistance. Second, center-tap biasing enables the ac voltage to have nearly zero common-mode voltage; this, in turn, results in an output signal from the bridge with nearly zero common-mode voltage, easing the readout circuitry.

In particular, readout is performed through a synchronous integrator involving a transistor and capacitor ($G_M - C$) by modulating the sensor output signal to a dc level (using a signal in-phase with the biasing voltage). By adjusting the integration time, aggressive filtering can be achieved of stray noise sources coupling to the sensors in the LAE domain. For digitization of the sensor output, the $G_M - C$ integrator is incorporated within a dual-slope analog-to-digital converter (ADC).

Aside from sensor readout, the sensing subsystem must support accessing of individual sensors within the subarray. As shown in Fig. 17, this is achieved using a-Si TFTs as accessing switches at each node of the full-bridge sensor. To robustly preserve of the sensor output signal, these switches must have low on resistance (i.e., large TFTs are needed), necessary to ensure minimal voltage drop of the biasing signal and minimal filtering of the output signal. In addition, circuitry to control the accessing switches (i.e., $EN\langle i \rangle$ signals) through a minimum number of interface signals is also necessary. This is achieved using a scanning circuit formed from a-Si TFTs [27]. Using three-phase control, the scanning circuit enables sequential accessing of each sensor in an arbitrarily large array, yet with just four interface signals (three control and one reset). The need for large accessing switches implies that the scanning circuit must drive substantial capacitance, making it the limiting factor setting the readout rate. As summarized in Section IV-E,

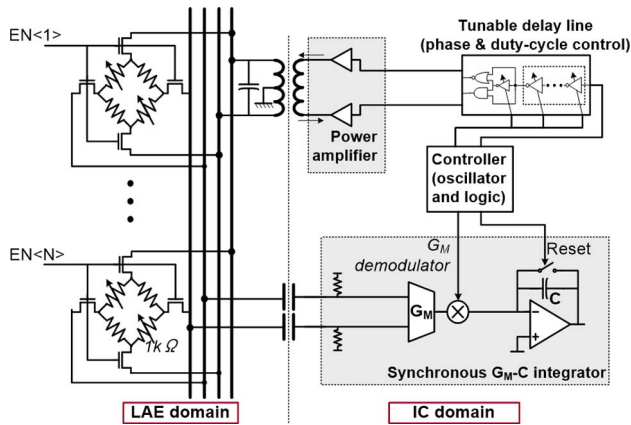


Fig. 17. Hybrid sensing subsystem.

the prototype sensing sheet preforms readout from the arrays of strain sensors at a rate of 500 Hz.

C. Power-Management Subsystem

Fig. 18 shows the details of the hybrid power-management subsystem [27]. A thin-film, flexible solar module is used for energy harvesting. As much of the remaining functionality as possible is preferably implemented in the CMOS domain, since the superior electrical characteristics of CMOS transistors enable greater current handling capability and lower switching/conduction losses. However, due to the use of noncontact (inductive and capacitive) interfaces, minimally power inversion (i.e., dc-to-ac conversion) is necessary in the LAE domain in order to couple the power harvested from the solar module in the LAE domain to the CMOS domain. Once received in the CMOS domain, required power rectification, under-voltage monitoring, over-voltage protection, and voltage conversion is readily achieved. Voltage conversion and regulation is performed using three embedded switch-capacitor dc/dc converters, which generate supply voltages of 0.6, 1.2, and 2.4 V, to power the entire system.

Though substantial power can be harvested by patterning large solar modules, power inversion in the LAE domain poses a critical challenge. The reason is limited power handling, due to low TFT currents, and low power-transfer efficiency, due to TFT conduction and switching losses in the power stage and control circuitry. The prototype sensing sheet employs the power-inverter topology proposed in [31]. The topology, shown in Fig. 19, is essentially a free-running inductor–capacitor (LC) oscillator, which provides power to the CMOS domain via coupling of planar tank inductors patterned on the sheet. The benefit of this topology is that it has no explicit control circuitry, mitigating control losses and leading to reasonable power-transfer efficiencies in practice (~30%). However, an additional concern is the output power level achievable by the inverter. The LC-oscillator topology has the benefit that, by exploiting the

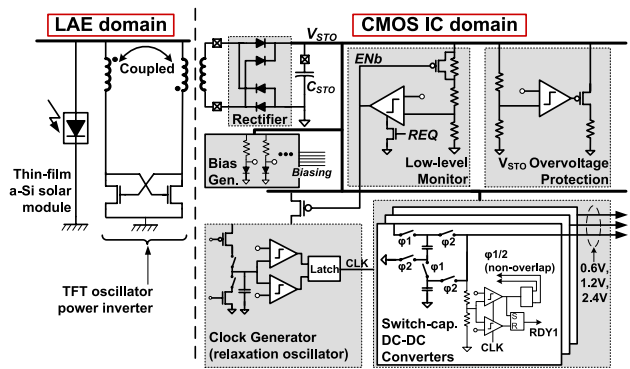


Fig. 18. Hybrid power-management subsystem based on solar energy harvesting and power inversion (dc-to-ac conversion) in the LAE.

turns ratio of the coupling inductors, the large voltages in the LAE domain (which can be tolerated by the TFTs) can be transformed into large currents in the CMOS domain. Thus, the current limitations of the TFTs can be overcome when providing power at the lower CMOS voltages. In this way, much greater power transfer is achieved (~22 mW).

The primary requirement for the LC-oscillator inverter topology to operate is that it must meet the positive-feedback oscillation condition [32]. This requires that the loop gain through the cross-coupled TFT stages exceed unity. As shown in Fig. 19, the oscillation condition depends partially on the TFT transconductance (g_m) and capacitances, but also on the quality factor of the tank. This, in turn, depends on the inductance and resistance of the planar inductors and the gate resistance of the TFTs. While the TFTs present poor transconductance and capacitances, the ability to pattern large planar spirals enables large inductances and low resistance, thus enabling the oscillation condition to be robustly met [31].

D. Communication Subsystem

The communication subsystem is responsible for communicating data (such as strain-gauge readings) among the CMOS ICs of various subarrays depicted in Fig. 15. This enables collaborative processing for damage

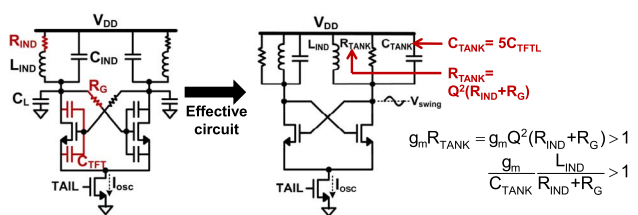


Fig. 19. LC-oscillator power inverter and associated oscillation condition.

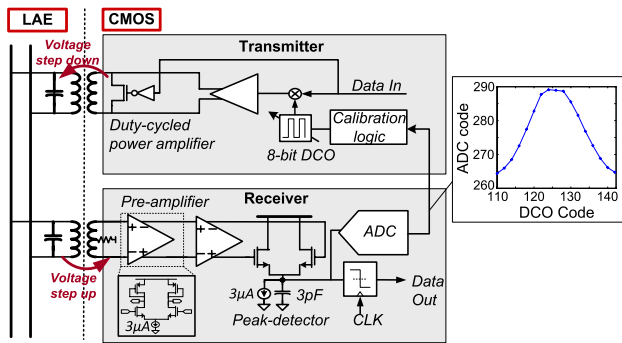


Fig. 20. Hybrid communication subsystem.

assessment and data aggregation for off-sheet communication by a centralized node on the sheet with wireless capability. Fig. 20 shows the details of the hybrid communication subsystem [27]. Wired interconnects are patterned on the sensing sheet to enable communication between the CMOS ICs of various subarrays. Each CMOS IC consists of a transceiver (transmitter and receiver). The signaling employed is on/off keying (OOK), wherein logic-1 pulses are modulated to a selected center frequency. The center frequency is chosen to coincide with the resonant frequency of the interconnect network. This enables strong voltage coupling across the inductive interface and makes the interconnect network appear as a large impedance, thus requiring minimal transmit power from the transceiver. Inductive interfaces between the CMOS transceiver and LAE interconnects are preferred to optimize the voltage amplitudes. Namely, at the transmitter, voltage setup down is preferred. This is because, at resonance, the resistance of the long interconnects can be modeled as a parallel resistor; smaller voltage amplitudes thus result in reduced power loss. On the other hand, at the receiver, voltage stepup is preferred, in order to maximize the receive signal-to-noise ratio (SNR). Roughly, the amplitude of the transmit pulse is 20 mV and that of the receive pulse is 40 mV.

The transmitter circuit shown in Fig. 20 consists of a digitally controlled oscillator (DCO) to generate the OOK carrier frequency and a class-C power amplifier. The receiver circuit consists of two stages of preamplifiers followed by a rectifier, whose output is taken from the source node of two coupled transistors, and finally a comparator. An important challenge in the communication subsystem is that the precise resonant frequency of the interconnect network is not known *a priori*. This necessitates a system-initiated frequency-calibration loop, where the transmitted signal is sensed off of the interconnect by the local receiver, and the DCO frequency is swept to the point of the maximum receive amplitude. This involves the use of an integrating ADC to digitize the receive amplitude. The ADC codes measured from the prototype during such a calibration are shown for illustration.

E. Prototype Characterization

The sensing sheet prototype was built, with LAE components fabricated in house and a CMOS IC fabricated in a commercial 130-nm CMOS process from IBM. The LAE components consist of TFT-based and metal-based strain gauges (10-element array), a flexible a-Si solar module on 50 μm -thick polyimide, and flexible a-Si TFT circuits on 50 μm -thick polyimide, all fabricated at 180 $^{\circ}\text{C}$ [33]. The prototype is shown on the top image of Fig. 21. For testing, the prototype was bonded to a cantilever beam in the lab using the methods of Section III. Additionally, commercially-available reference strain gauges were bonded to the beam at locations in proximity to specific strain sensors on the sheet, and were read out using a commercial system (Vishay 3800) to provide controlled comparison. For strain measurement characterization of the prototype, the beam was subjected to controlled strain, as shown in the bottom of Fig. 21.

Details of the measurements and characterization are provided in [20], [21], and [27], and a summary is provided in Table 2. As shown, a strain-readout sensitivity of 18 $\mu\epsilon_{\text{RMS}}$ and maximum nonlinearity of 21 $\mu\epsilon$ is achieved, exceeding the requirement specifications derived in Section III. The energy per measurement, including sensor accessing control and sensor readout (acquisition and digitization) is 434 nJ at a maximum measurement rate of 500 Hz. Given a total solar module size of 300 cm^2 (with output power level between 10 μW and 10 mW depending on the illumination conditions), and >30% power-transfer efficiency to the CMOS IC by the LAE power inverter, adequate power harvesting is achieved for frequent measurements over large strain-gauge arrays. Within the CMOS domain, the overall power-conversion efficiency for generating the on-chip supplies is over 80%. Though the system represents a relatively small-scale prototype, it demonstrates the sensitivity and power levels required for the proposed sensing approach, as analyzed in Section III.

V. CONCLUSION AND FUTURE WORK

This paper identified the need for a 2-D array of strain sensors for damage characterization over large areas of civil structures and infrastructure. Technologically, this motivates a sensing sheet that is based on LAE and CMOS ICs. The damage detection, localization, and evaluation capabilities of such a technology are analyzed.

Analysis over several research stages is presented. Laboratory testing of the unit sensor installed on a concrete specimen led to the conclusion that the sensor can survive 1.5-mm crack opening and its output can be used to statistically evaluate the crack width. Analysis of geometrical arrangements of the unit sensors within the sensing sheet has shown that symmetric equidistant arrangement provides the highest POD. Also, the POD

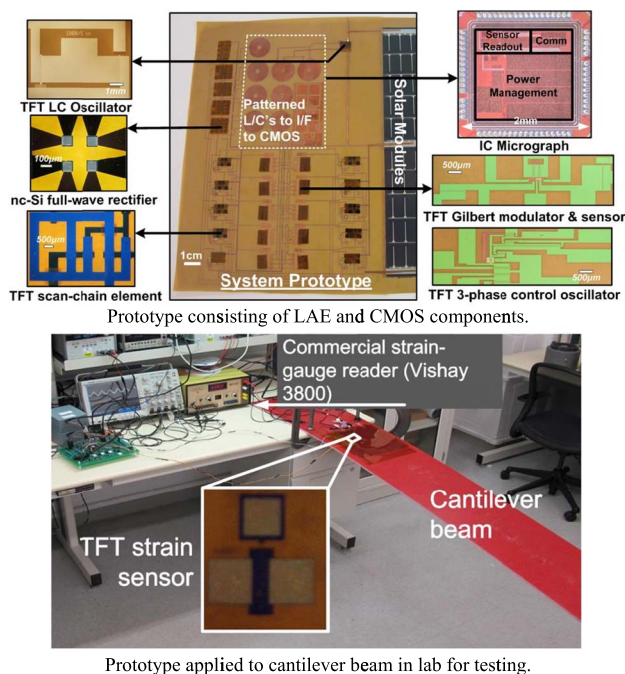


Fig. 21. Self-powered sensing sheet prototype.

strongly depends on the number of the sensors within the sheet, and for a given number of sensors the POD limits at a constant value for a certain crack length, called the critical crack length. Cycling fatigue tests led to the conclusion that the POD is actually higher in real-life situations compared to that analytically calculated, due to notable damage detection capability of sensors that are not in direct contact with the damage. These additional sensors can detect the damage through a negative change in strain if they are close enough to the damage (in the tests, typically 10–20 mm far from damage). Malfunction of several sensors did not affect the overall damage characterization capabilities of the sensing sheet, demonstrating its robustness for damage characterization. Thus, the cycling fatigue tests validated the

direct-sensing approach, and demonstrated that a sensing sheet can detect the damage, follow its propagation, and evaluate its extent even if some unit sensors experience malfunction.

A proof-of-concept hybrid sensing sheet based on LAE and CMOS ICs has been demonstrated, enabling evaluation both of strain-measurement accuracy and system-level operation (energy consumption, robustness, data communication, etc.). To enhance scalability of the hybrid system, noncontact (inductive/capacitive) interfaces are employed between the LAE and CMOS technology domains, enabling system assembly simply via sheet lamination. The demonstrated system is self-powered using a thin-film a-Si solar module in the LAE domain, with power transferred to the CMOS domain inductively via a TFT-based power inverter. Strain sensing is performed using two types of strain gauges in the LAE domain: full-bridge metal strain gauges exhibiting resistive response, and a-Si strain gauges exhibiting mobility response (the former being analyzed in detail in beginning part of the paper). The prototype system demonstrates strain-readout sensitivity of better than $18 \mu\epsilon_{RMS}$, at an energy per measurement of 434 nJ and maximum measurement rate of 500 Hz. The performance exceeds the presented requirements developed from laboratory experiments. Further development of a large-scale sensing sheet, first for laboratory testing and then for on-bridge deployment and testing, is being pursued. ■

Acknowledgment

The authors would like to thank R. Betti, Liming Li and E. Sporer from Columbia University for accommodating the cycling tests, T. Schumacher, A. Shariati, A. Tabrizi, and Lassaad Mhamdi from University of Delaware for providing steel plates and associated equipment, and Y. Hu, J. Sanz Robinson, L. Huang, T. Moy, W. Rieutort-Louis, D. Smith, and J. Vocaturo from Princeton University for various contributions to technology demonstration and testing.

Table 2 Characterization of the Sensing Sheet Prototype

Performance summary			
Technology			
LAE	a-Si on 50µm polyimide @ 180 °C		
CMOS IC	130nm CMOS		
Power Management Subsystem			
TFT Power Inverter η	30%	DC-DC output voltages	0.6V, 1.2V, 2.4V
Solar Module Size	300cm ²	Overall DC-DC converter η	80.5%
Sensing Subsystem (piezoresistive sensor)			
Max. Readout Noise	17.9µε _{RMS}	Max. Readout Non-linearity	20.7µε _{RMS}
Total Energy/meas,	434nJ	Max. Measurement/sec.	500
Communication Subsystem			
Tx Energy (@7.5)	14.6pJ/bit	Max. Data Rate	2Mb/s
Rx Energy (@7.5)	4.3pJ/bit	Self-calibration Loop Energy	17µJ

REFERENCES

- [1] B. Glisic and D. Inaudi, "Introduction to structural health monitoring," in *Fiber Optic Methods for Structural Health Monitoring* xth. Chichester, U.K.: Wiley, 2007 ch. 1.1.1, pp. 1–10.
- [2] C. R. Farrar and K. Worden, "An introduction to structural health monitoring," *Philosoph. Trans. Roy. Soc. A, Math. Phys. Eng. Sci.*, vol. 365, no. 1851, pp. 303–315, 2007.
- [3] A. Rytter, "Vibrational based inspection of civil engineering structures," Ph.D. dissertation Dept. Building Technol. Struct. Eng., Aalborg Univ., Aalborg, Denmark, 1993.
- [4] Y. Yao and B. Glisic, "Reliable damage detection and localization using direct strain sensing," in *Proc. 6th Int. IAMBAS Conf. Bridge Maintenance Safety Manage.*, Stresa, Italy, 2012, pp. 714–721.
- [5] D. Posenato, F. Lanata, D. Inaudi, and I. F. C. Smith, "Model-free data interpretation for continuous monitoring of complex structures," *Adv. Eng. Inf.*, vol. 22, no. 1, pp. 135–144, 2008.
- [6] B. Glisic and N. Verma, "Very dense arrays of sensors for SHM based on large area electronics," in *Proc. 8th Int. Workshop Struct. Health Monitoring*, 2011, vol. 2, pp. 1409–1416.
- [7] D. Hubbell and B. Glisic, "Detection and characterization of early age thermal cracks in high performance concrete," *ACI Mater. J.*, vol. 110, no. 3, pp. 323–330, 2013.
- [8] H. Abdel-Jaber and B. Glisic, "Analysis of the status of pre-release cracks in prestressed concrete structures using long-gauge sensors," *Smart Mater. Struct.*, vol. 24, 2015, Art. no. 025038.
- [9] J. P. Lynch and T.-C. Hou, "Conductivity-based strain and damage monitoring of cementitious structural components," *Proc. SPIE—Int. Soc. Opt. Eng.*, vol. 5765, pp. 419–429, 2005.
- [10] K. J. Loh, T.-C. Hou, J. P. Lynch, and N. A. Kotov, "Carbon nanotube sensing skins for spatial strain and impact damage identification," *J. Nondestruct. Eval.*, vol. 28, pp. 9–25, 2009.
- [11] M. Hallaji, A. Seppänen, and M. Pour-Ghaz, "Electrical impedance tomography-based sensing skin for quantitative imaging of damage in concrete," *Smart Mater. Struct.*, vol. 23, 2014, Art. no. 085001.
- [12] T. Schumacher and E. T. Thostenson, "Development of structural carbon nanotube-based sensing composites for concrete structures," *J. Intell. Mater. Syst. Struct.*, vol. 25, no. 11, pp. 1331–1339, Jul. 2014.
- [13] N. Sharp et al., "A bio-inspired asynchronous skin system for crack detection applications," *Smart Mater. Struct.*, vol. 23, 2014, Art. no. 0550205.
- [14] S. Laflamme et al., "Soft elastomeric capacitor network for strain sensing over large surfaces," *IEEE/ASME Trans. Mechatron.*, vol. 18, pp. 1647–1654, 2013.
- [15] P. A. Withey, V. S. M. Vemuru, S. M. Bachilo, S. Nagarajiah, and R. B. Weisman, "Strain paint: Noncontact strain measurement using single-walled carbon nanotube composite coatings," *Nano Lett.*, vol. 12, no. 7, pp. 3497–3500, 2012.
- [16] D. Zonta et al., "Photonic crystals for monitoring fatigue phenomena in steel structures," *Proc. SPIE—Int. Soc. Opt. Eng.*, vol. 7292, 2009, Art. no. 729215.
- [17] N. P. Salowitz et al., "Microfabricated expandable sensor networks for intelligent sensing materials," *IEEE Sens. J.*, vol. 14, no. 7, pp. 2138–2144, 2014.
- [18] Y. Hu et al., "High-resolution sensing sheet for structural health monitoring via scalable interfacing of flexible electronics with high-performance ICs," in *Proc. IEEE Symp. VLSI Circuits*, Jun. 2012, pp. 120–121.
- [19] S.-T. Tung, Y. Yao, and B. Glisic, "Sensing sheet: The sensitivity of thin-film full-bridge strain sensors for crack detection and characterization," *Meas. Sci. Technol.*, vol. 25, no. 7, 2014, Art. no. 075602.
- [20] Y. Hu et al., "Large-scale sensing system combining large-area electronics and CMOS ICs for structural-health monitoring," *IEEE J. Solid-State Circuits*, vol. 49, no. 2, pp. 1–12, 2014.
- [21] N. Verma et al., "Enabling scalable hybrid systems: Architectures for exploiting large-area electronics in applications," *Proc. IEEE*, vol. 103, no. 4, pp. 690–712, Apr. 2015.
- [22] T. Someya, B. Pal, J. Huang, and H. E. Katz, "Organic semiconductor devices with enhanced field and environmental responses for novel applications," *MRS Bull.*, vol. 33, pp. 690–696, 2008.
- [23] L. Zhou, S. Jung, E. Brandon, and T. Jackson, "Flexible substrate micro-crystalline silicon and gated amorphous silicon strain sensors," *IEEE Trans. Electron Devices*, vol. 53, no. 2, pp. 380–385, 2006.
- [24] T. Someya et al., "A large-area, flexible pressure sensor matrix with organic field-effect transistors for artificial skin applications," *Proc. Nat. Acad. Sci.*, vol. 101, pp. 9966–9970, 2004.
- [25] N. T. Jafferis and J. C. Sturm, "Fundamental and experimental conditions for the realization of traveling-wave-induced aerodynamic propulsive forces by piezoelectrically deformed plastic substrates," *J. Microelectromech. Syst.*, vol. 22, no. 2, pp. 495–505, 2013.
- [26] Y. Qi et al., "Piezoelectric ribbons printed onto rubber for flexible energy conversion," *Nano Lett.*, vol. 10, pp. 524–528, 2010.
- [27] Y. Hu et al., "Self-powered system for large-scale strain sensing by combining CMOS ICs with large-area electronics," *IEEE J. Solid-State Circuits*, vol. 49, no. 4, pp. 838–850, 2014.
- [28] A. Coppe, R. T. Haftka, and N. Kim, "Optimization of distribution parameters for estimating probability of crack detection," *J. Aircraft*, vol. 46, no. 6, pp. 2090–2097, 2009.
- [29] Y. Yao and B. Glisic, "Sensing sheets: Optimal arrangement of dense array of sensors for an improved probability of damage detection," *Struct. Health Monitoring*, vol. 4, no. 5, pp. 513–531, 2015.
- [30] Y. Yao and B. Glisic, "Detection of steel fatigue cracks with strain sensing sheets based on large area electronics," *Sensors*, vol. 15, pp. 8088–8108, 2015.
- [31] Y. Hu et al., "Flexible solar-energy harvesting system on plastic with thin-film LC oscillators operating above ft for inductively-coupled power delivery," in *Proc. IEEE Custom Integr. Circuits Conf.*, Sep. 2012, doi: 10.1109/CICC.2012.6330627.
- [32] B. Razavi, *Design of Analog CMOS Integrated Circuits*. New York, NY, USA: McGraw-Hill, 2001.
- [33] B. Hekmatshoar et al., "Highly stable amorphous-silicon thin-film transistors on clear plastic," *Appl. Phys. Lett.*, vol. 93, 2008, Art. no. 032103.

ABOUT THE AUTHORS

Branko Glišić received the bachelor degrees in civil engineering (B.C.E.) and theoretical mathematics (B.Math.) from the University of Belgrade, Belgrade, Serbia and the Ph.D. degree from the EPFL, Zurich, Switzerland.



After eight-year long experience at SMART-TEC SA, Switzerland, where he was involved in numerous SHM projects, he has been employed, first as an Assistant Professor, and currently as an Associate Professor at the Department of Civil and Environmental Engineering, Princeton University, Princeton, NJ, USA. He is an author and coauthor of more than 100 published papers, short courses on SHM, and the book *Fiber Optic Methods for Structural Health Monitoring* (New York, NY, USA: Wiley, 2007). His vision is a ubiquitous and pervasive deployment of structural health monitoring (SHM) of civil structures and

infrastructure, and his main areas of interest are SHM methods, advanced sensors based on fiber optics, large-area electronics and conductive polymers, SHM data management and analysis, smart structures, and heritage structures.

Prof. Glišić received the 2013 SHM Person of the Year Award by the editors and associate editors of *Structural Health Monitoring: An International Journal*, as well as several other awards. He is Vice President and Council Member of the International Society for Structural Health Monitoring of Intelligent Infrastructure (ISHMII), Editor-in-Chief of ISHMII's newsletter *The Monitor*, and member of several other professional associations such as the American Concrete Institute (ACI), the International Association for Bridge and Structural Engineers (IABSE), the American Society of Civil Engineers (ASCE), the International Association for Bridge Maintenance and Safety (IABMAS), etc., and journal editorial boards (*Advances in Structural Engineering*, *Structural Monitoring and Maintenance*, and *Frontiers in Built Environment*).

Yao Yao received the B.S. degree in civil engineering from Harbin Institute of Technology, China, in 2010 and the Ph.D. degree in civil engineering from Princeton University, Princeton, NJ, USA, in 2015.

He is an author and coauthor of more than 30 published papers. His research interests include structural health monitoring (SHM) and structural analysis, SHM methods and strategies, fiber optic sensors (FOS) and advanced sensing technologies based on large area electronics (LAE).

Dr. Yao was awarded the China Civil Engineering Society Outstanding College Graduate Award and the Princeton University Fellowship in 2010, was supported by the National Science Foundation to attend the Asian-Pacific Summer School (APSS) in India in 2012, and was awarded the Wu Prize for Excellence by Princeton University in 2014. He is a student member of the American Society of Civil Engineers (ASCE) and the International Society for Structural Health Monitoring of Intelligent Infrastructures (ISHMII).



Shue-Ting E. Tung received the B.S. degree in engineering in civil and environmental engineering from Princeton University, Princeton, NJ, USA and the M.S. degree in civil and environmental engineering from Stanford University, Stanford, CA, USA.

She currently works in construction management at Pankow Builders Ltd., a general contractor in California. During her time at Princeton, she became interested in structural health monitoring and performed extensive junior and senior research on direct sensing techniques, resulting in several journal publications and conference presentations.

Miss Tung is a recipient of Princeton's The Tau Beta Pi Prize and W. Mack Angas Prize.



Sigurd Wagner (Fellow, IEEE) received the Ph.D. degree from the University of Vienna, Vienna, Austria.

Following a Postdoctoral Fellowship at Ohio State University, Columbus, OH, USA, he worked from 1970 to 1978 at the Bell Telephone Laboratories in Murray Hill and Holmdel, NJ, USA, on semiconductor memories and heterojunction solar cells. He then joined the Solar Energy Research Institute (now NREL), Golden, CO, USA, as the founding Chief of the Photovoltaic Research Branch. Since 1980, he has been Professor of Electrical Engineering at Princeton University, Princeton, NJ, USA; in 2015 he became Professor Emeritus and Senior Scholar. He has been developing fundamentally new materials, processes, and components for flexible large-area electronics, electrotextiles, and electronic skin, and is considered the father of soft elastic electronics.



James C. Sturm (Fellow, IEEE) was born in Berkeley Heights, NJ, USA, in 1957. He received the B.S.E. degree in electrical engineering and engineering physics from Princeton University, Princeton, NJ, USA, in 1979 and the M.S.E.E. and Ph.D. degrees from Stanford University, Stanford, CA, USA, in 1981 and 1985, respectively.

In 1979, he joined Intel Corporation, Santa Clara, CA, USA, as a Microprocessor Design Engineer, and in 1981, he was a Visiting Engineer at Siemens, Munich, Germany. In 1986, he joined the faculty of Princeton University, where he is currently the Stephen R. Forrest Professor in Electrical Engineering. From 1998 to 2015, he was the Director of the Princeton Photonics and Optoelectronic Materials Center (POEM) and its successor, the Princeton Institute for the Science and Technology of Materials (PRISM). In 1994-1995, he was a von Humboldt Fellow at the Institut fuer Halbleitertechnik, University of Stuttgart, Stuttgart, Germany. He has worked in the fields of silicon-based heterojunctions, thin-film and flexible electronics, photovoltaics, the nanobiointerface, 3-D integration, and silicon-on-insulator.

Dr. Sturm has won over ten awards for teaching excellence and was a National Science Foundation Presidential Young Investigator. In 1996 and 1997, he was the Technical Program Chair and General Chair of the IEEE Device Research Conference, respectively. He served on the organizing committee of IEDM (1988 to 1992 and 1998 to 1999), having chaired both the solid-state device and detectors/sensors/displays committees. He has served on the boards of directors of the Materials Research Society and the Device Research Conference, and cofounded Aegis Lightwave and SpaceTouch.



Naveen Verma (Member, IEEE) received the B.A.Sc. degree in electrical and computer engineering from the University of British Columbia, Vancouver, BC, Canada, in 2003 and the M.S. and Ph.D. degrees in electrical engineering from Massachusetts Institute of Technology, Cambridge, MA, USA, in 2005 and 2009, respectively.

Since July 2009 he has been with the Department of Electrical Engineering, Princeton University, Princeton, NJ, USA, where he is currently an Associate Professor. His research focuses on advanced sensing systems, including low-voltage digital logic and SRAMs, low-noise analog instrumentation and data-conversion, large-area sensing systems based on flexible electronics, and low-energy algorithms for embedded inference, especially for medical applications.

Prof. Verma serves on the technical program committees for ISSCC, VLSI Symposium On Circuits, and IEEE Signal-Processing Society (DISPS). He is a recipient or corecipient of the 2006 DAC/ISSCC Student Design Contest Award, the 2008 ISSCC Jack Kilby Paper Award, the 2012 Alfred Rheinsein Junior Faculty Award, the 2013 NSF CAREER Award, the 2013 Intel Early Career Award, the 2013 Walter C. Johnson Prize for Teaching Excellence, the 2013 VLSI Symposium Best Student Paper Award, the 2014 AFOSR Young Investigator Award, the 2015 Princeton Engineering Council Excellence in Teaching Award, and the 2015 IEEE Transactions on Components, Packaging and Manufacturing Technology Best Paper Award.

